TurBot: A Turtle-Inspired Quadruped Robot Using Topology Optimized Soft-Rigid Hybrid Legs

Yilun Sun, *Member, IEEE*, Felix Pancheri, Christoph Rehekampff, and Tim C. Lueth, *Senior Member, IEEE*

***Abstract*—Quadruped robots are used for a wide variety of transportation and exploration tasks due to their high dexterity. Currently, many studies utilize soft robotic legs to replace rigid-link-based legs, with the aim to improve quadruped robots' adaptability to complex environments. However, the conventional soft legs still face the challenge of limited load-bearing capacity. To cope with this issue, we propose in this work a type of soft-rigid hybrid leg, which is synthesized by using a multistage topology optimization method. A simplified model is also created to describe the kinematics of the synthesized soft leg. Using the realized legs, we have developed a turtle-inspired quadruped robot called TurBot. By mimicking the walking pattern of a turtle, two motion gaits (straight-line walking and turning) are designed to realize the robotic locomotion. Experiments are also conducted to evaluate the walking performance of TurBot. Results show that the realized robot can achieve stable straight-line walking and turning motions. In addition, TurBot can carry up to 500 g extra weight while walking, which is 126% of its own body weight. Moreover, different locomotion tests have also successfully verified TurBot's ability to adapt to complex environments.**

***Index Terms*—Bio-inspired locomotion robot, quadruped robot, soft-rigid hybrid leg, topology optimization.**

I. Introduction

IN RECENT years, quadruped robots have been extensively researched due to their high flexibility and excellent performance in traversing complex terrains [1]. For instance, a multimodal quadruped robot ALPHRED was developed in [2] to enable flexible package delivery in different scenarios. By integrating a learning-based controller, the ANYmal robot can perform blind locomotion in challenging terrains [3]. Since the concept of quadruped robots originated from four-legged animals, their robotic structures usually have a bionic design. For example, the robots in [4] and [5] took inspiration from mammals such as dogs and rats due to their compact structure and good dynamic performance. Other robots [6], [7] are inspired by reptiles such as crocodiles and turtles because their bodies have a more stable supporting polygon.

In conventional quadruped robots, rigid-link legs with motors mounted on their rotation joints are usually used to perform robotic locomotion [6], [8]. Despite their high structural stiffness, those rigid-link legs still have limitations because their rotational joints are subjected to large forces or impacts during locomotion, which may damage the motors mounted on the joints. To cope with this problem, many research studies have introduced underactuated or soft robotic leg structures in order to absorb the external forces through compliant mechanism. For instance, springs and dampers were integrated in the redundant leg structures of the Cheetah-cub robot [9] and the ScarlETH leg [10] to improve their walking stability. Tolley et al. [11] developed a pneumatically driven soft quadruped robot without any rigid components using silicone-rubber-made legs. By combining a precharged pneumatic structure with a cable-driven mechanism, the authors in [4] have created amphibious soft robotic legs that enable a robotic dog to perform walking and swimming motions. Other studies [12], [13] also used 3-D printing technology to fabricate soft legs for flexible locomotion of quadruped robots. However, despite the high structural compliance of purely soft robotic structures, they still face the challenge of limited load-bearing capacity. From this point of view, soft robotic leg structures with balanced bending flexibility and structural stiffness (i.e., soft-rigid hybrid feature) are highly desirable.

In current research, topology optimization methods have become a popular approach to achieve the structural design of soft robots [14], as they can automatically generate robotic structures according to specific design requirements. Liu et al. [15] proposed a 2-D topology optimization method to synthesize soft fingers for a motor-driven gripper. Another soft robotic gripper was designed by Sun et al. [16] using a 3-D topology optimization method. In addition, the authors in [17] successfully achieved topology optimized soft actuators with pneumatic actuation. Moreover, recent studies also tried to synthesize soft-rigid hybrid structures using topology optimization methods. For example,

Manuscript received 20 January 2024; revised 21 March 2024; accepted 19 May 2024. Date of publication 6 June 2024; date of current version 16 August 2024. This work was supported by the TUM School of Engineering and Design, Technical University of Munich, Germany. Recommended by Technical Editor B. Shyrokau and Senior Editor Q. Zou. *(Corresponding author: Yilun Sun.)*

The authors are with the Institute of Micro Technology and Medical Device Technology, Technical University of Munich, 85748 Garching, Germany (e-mail: yilun.sun@tum.de; felix.pancheri@tum.de; christoph.rehekampff@tum.de; tim.lueth@tum.de).

This article has supplementary material provided by the authors and color versions of one or more figures available at https://doi.org/10.1109/TMECH.2024.3404667.

Digital Object Identifier 10.1109/TMECH.2024.3404667

Fig. 1. Turtle-inspired quadruped robot (TurBot) walking in a park.

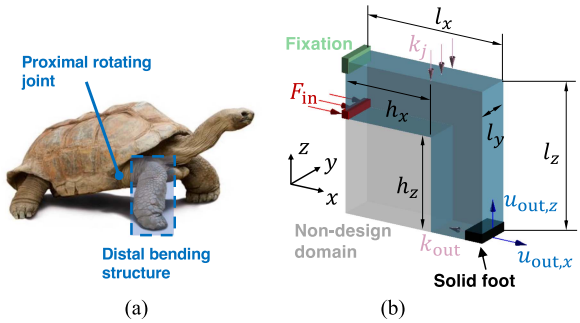

Fig. 2. (a) Structure of the leg of a land turtle. (b) Schematic diagram illustrating the topology optimization problem in Design stage I for synthesizing the bending leg structure.

a multiobjective topology optimization method was developed in [18] to create flexure joints with balanced rotational flexibility and torsional stiffness. Another topology-optimization-based approach was proposed in [19] to adjust the multiaxis stiffness of soft robotic joints. Nevertheless, only a few research works [20] were working on topology optimized soft leg structures.

In this article, we present a turtle-inspired quadruped robot (TurBot) with topology optimized soft-rigid hybrid legs. As is shown in Fig. 1, the robot is 3-D printed and can perform flexible locomotion in complex environments. This work has the following contributions.

1) Development of a multistage topology optimization method for designing the soft-rigid hybrid leg. Design stage I is used to realize a soft leg structure, while Design stage II achieves the optimal soft-rigid hybrid feature by optimizing the leg volume fraction.
2) Kinematic modeling of the synthesized soft-rigid hybrid leg using a simplified two-Degree-of-Freedom (2-DOF) rigid-link model.
3) Turtle-inspired gait design for the straight-line walking and turning motions.
4) Experimental evaluation of TurBot's walking performance in different environments.

The rest of this article is organized as follows. Section II describes the design process of the soft-rigid hybrid leg. The kinematic modeling and motion gait design of TurBot are presented in Section III. In Section IV, experiments are conducted to evaluate the walking performance of the developed robot. Finally, Section V concludes this article.

II. Design of Soft-Rigid Hybrid Leg

A. Design Stage I: Topology-Optimization-Based Synthesis of Soft Leg Structure

In this work, by mimicking the anatomy of a turtle's leg [see Fig. 2(a)], each leg of the robot consists of a proximal rotating joint and a distal bending structure. In the first design stage, we used a topology optimization approach [16] to synthesize a soft robotic structure for achieving the distal bending motion.

As is shown in Fig. 2(b), the basic principle of the utilized topology optimization method is to iteratively modify the density distribution of a finite-element-based (FE-based) design domain to achieve specific output motion directions under a certain load. Here, we used a $N_x \times N_y \times N_z$ voxel model with N_e cubic elements ($N_e = N_x \cdot N_y \cdot N_z$) to construct the design domain. Since the realized soft robotic structure is subject to large-displacement deformations, a geometrically nonlinear FE analysis approach [21] was employed to determine the displacements of the N_n nodes in the voxel model [$N_n = (N_x + 1) \cdot (N_y + 1) \cdot (N_z + 1)$]. The mathematical formulation of the FE analysis can be generalized as follows:

$$\mathbf{r} = \mathbf{F}_{\text{ext}} - \mathbf{F}_{\text{int}}(\mathbf{u}) = \mathbf{0} \tag{1}$$

$$\mathbf{F}_{\text{int}}(\mathbf{u}) = \int_{\mathbf{u}} \mathbf{K}(\mathbf{u})\,\mathbf{du} \quad \text{with} \quad \mathbf{K}(\mathbf{u}) = \sum_{e=1}^{N_e} x_e^p \cdot \mathbf{k_e}(\mathbf{u}) \tag{2}$$

where $\mathbf{u}$ represents the displacement vector ($3N_n \times 1$) that can be solved by using a Newton–Raphson approach. $\mathbf{F}_{\text{ext}}$ and $\mathbf{F}_{\text{int}}$ are the external and internal load vectors with the dimension $3N_n \times 1$, whereas $\mathbf{r}$ is the residual load vector. As is shown in (2), $\mathbf{F}_{\text{int}}$ can be obtained by accumulating the internal stresses during the large-displacement deformation, where $\mathbf{K}(\mathbf{u})$ is the intermediate global stiffness matrix with the dimension $3N_n \times 3N_n$. In order to modify the material stiffness of $\mathbf{K}(\mathbf{u})$ during the topology optimization process, a variable density $x_e \in [x_{\min}, 1]$ is introduced for each element to correct the elemental stiffness matrix $\mathbf{k_e}(\mathbf{u})$. Here, $x_{\min} = 10^{-6}$ is a minimum density value for preventing singularity problems in FE analysis, while the penalty factor $p = 3$ is used to regulate the optimization speed.

The optimization problem in the first design stage can be described mathematically as follows:

$$\left.\begin{array}{ll} \min_{\mathbf{x}} & : g_1(\mathbf{x}) = \mathbf{L}^{\mathbf{T}}\mathbf{u_1} = -u_{\text{out,x}} - u_{\text{out,z}} \\ \text{s.t.} & : \mathbf{r_1}(\mathbf{F}_{\text{ext,1}}, \mathbf{u_1}, \mathbf{x}) = \mathbf{0} \\ & : \mathbf{K_1}(\mathbf{u_1}) = \mathbf{K_s}(k_j, k_{\text{out}}) + \sum_{e=1}^{N_e} x_e^p \cdot \mathbf{k_e}(\mathbf{u_1}) \\ & : \sum_{e=1}^{N_e} x_e \cdot \frac{v_e}{V_0} \le \gamma \end{array}\right\}. \tag{3}$$

Similar to the lifting motion pattern of a turtle leg, the design objective of (3) is to maximize the output displacement ($u_{\text{out,x}} + u_{\text{out,z}}$) of the bending leg structure under a predefined load vector $\mathbf{F}_{\text{ext,1}}$. Herein, $\mathbf{L}$ is a $3N_n \times 1$ sparse vector for searching $u_{\text{out,x}}$ and $u_{\text{out,z}}$ from the displacement vector $\mathbf{u_1}$, whereas $\mathbf{x}$ is a $N_x \times$

$N_y \times N_z$ density model containing the x_e of all elements. In order to create a soft leg structure with distributed compliance, we have incorporated an artificial spring k_j into the leg joint area of the design domain (in addition to the default output spring k_{out}). $\mathbf{K_s}$ is the stiffness matrix of the added springs. Moreover, a volume fraction factor γ is also introduced to constrain the volume of the realized bending leg structure, where v_e/V_0 is the volume ratio of a single element to the entire design domain.

The detailed boundary conditions for the optimization problem in (3) are also illustrated by Fig. 2(b). It can be seen that, the blue area in the figure represents the design domain with modifiable x_e, whereas a nondesign void domain (gray area with $x_e = x_{\min}$) is set to ensure a certain obstacle-climbing height of the leg. In addition, a solid foot domain (black area with $x_e = 1$) is introduced to generate sufficient contact area with the ground, and the foot tip is defined as the output port. On the other hand, the green box in Fig. 2(b) shows the fixed area of the design domain, and the red arrows indicate the application position and direction of the input force F_{in} (used to create $\mathbf{F}_{\text{ext},1}$). The added artificial springs are denoted by the pink arrows.

To achieve the iterative update of $\mathbf{x}$, we should first conduct sensitivity analysis on the objective function $g_1(\mathbf{x})$. According to (3), the derivative of $g_1(\mathbf{x})$ with respect to x_e can be formulated as follows:

$$\frac{\partial g_1}{\partial x_e} = \mathbf{L}^{\mathbf{T}} \frac{\partial \mathbf{u_1}}{\partial x_e}. \tag{4}$$

By taking the derivative of $\mathbf{r_1} = \mathbf{0}$ with respect to x_e, the value of $\partial/\mathbf{u_1}\partial x_e$ can be calculated as follows:

$$\frac{\mathrm{d}\mathbf{r_1}}{\mathrm{d}x_e} = \frac{\partial \mathbf{r_1}}{\partial \mathbf{u_1}} \frac{\partial \mathbf{u_1}}{\partial x_e} + \frac{\partial \mathbf{r_1}}{\partial x_e} = \mathbf{0} \Rightarrow \frac{\partial \mathbf{u_1}}{\partial x_e} = \mathbf{K_T^{-1}} \cdot \frac{\partial \mathbf{r_1}}{\partial x_e} \tag{5}$$

where $\mathbf{K_T} = -\partial/\mathbf{r_1}\partial\mathbf{u_1}$ is the symmetrical tangent stiffness matrix of $\mathbf{r_1}$. Hence, $\partial g_1/\partial x_e$ can be obtained by substituting (5) into (4) as follows:

$$\frac{\partial g_1}{\partial x_e} = (\mathbf{K_T^{-1}} \cdot \mathbf{L})^{\mathbf{T}} \frac{\partial \mathbf{r_1}}{\partial x_e}. \tag{6}$$

With the sensitivity analysis result in (6), a standard optimality criterion method [22] was employed in this work to update $\mathbf{x}$ iteratively as follows:

$$x_{\text{e,new}} = x_e \cdot \left(\frac{-\frac{\partial g_1}{\partial x_e}}{\lambda v_e} \right)^{\eta} \quad \text{with} \quad x_{\text{e},0} = \gamma \tag{7}$$

where $x_{\text{e},0}$ and $x_{\text{e,new}}$ represent the initial density and the updated density, respectively. $\eta = 0.3$ is a damping coefficient while λ is a Lagrangian multiplier that can be determined via a bisection method [22]. Moreover, the sensitivity-based filter from [22] is introduced to suppress the potential checkerboard patterns during the topology optimization process. The density update process ends when the iterative change in $|g_1(\mathbf{x})|$ is less than 0.01%. After that, the isosurface method is used to create an stereolithography (STL)-file of the optimized density model for additive manufacturing. In this work, the optimization algorithms and the geometry modeling processes were implemented in MATLAB using the Solid Geometry Library [23].

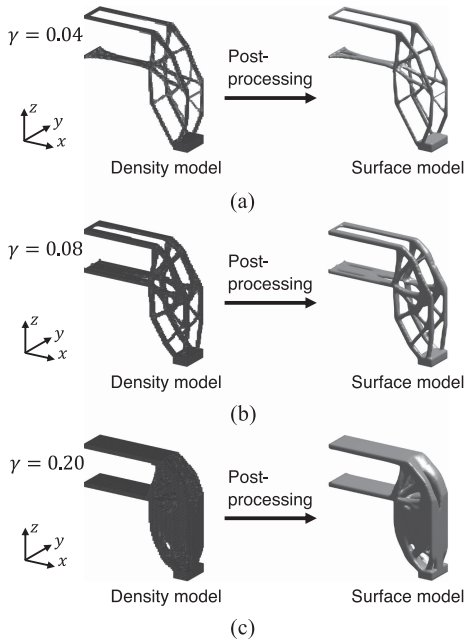

Fig. 3. Synthesis results of the bending leg structure with different γ values. The black elements in the optimized density model represent $x_e = 1$. (a) $\gamma = 0.04$. (b) $\gamma = 0.08$. (c) $\gamma = 0.20$.

TABLE I
OPTIMIZATION PARAMETERS USED IN DESIGN STAGE I

Parameter	Symbol	Value
Length of design domain in x axis	l_x	40 mm
Length of design domain in y axis	l_y	10 mm
Length of design domain in z axis	l_z	40 mm
Length of non-design domain in x axis	h_x	25 mm
Length of non-design domain in z axis	h_z	25 mm
Number of elements in the voxel model	N_e	128 000
Input force	F_{in}	1 N
Spring at the leg joint area	k_j	0.5 N/mm
Spring at the output port	k_{out}	0.5 N/mm
Elastic modulus (PA2200)	E_0	1700 MPa
Poisson's ratio	ν	0.3

Fig. 3 shows several synthesis results for the first design stage, where different γ values were used in the optimization for comparison. Here, the main dimension of the design domain (l_z) was chosen as 40 mm in order to allow the realized leg to climb over obstacles of 20 mm. Other related design parameters are listed in Table I. It can be seen from Fig. 3 that, for all γ values, the optimized bending leg structure is generally composed of multiple parallel flexible beams and a rigid foot structure, which presents a good combination of bending flexibility and standing stiffness. Here, the emergence of this soft-rigid hybrid feature can be attributed to the artificial spring k_j added to the optimization problem, as it introduced additional structural compliance to the leg joint area [16]. In addition, it can also be noticed from Fig. 4 that the absolute value of the optimized g_1 decreases as the γ value increases. This suggests that while an increase in leg volume results in stronger legs, it also reduces their bending flexibility. Based on this phenomenon, we proposed a second design stage to further optimize the γ value, in order to achieve the most balanced soft-rigid hybrid performance of the leg.

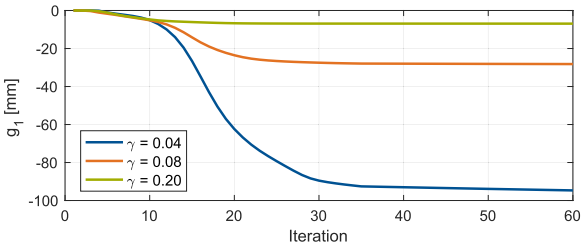

Fig. 4. Iteration history of the objective function g_1 for different γ values.

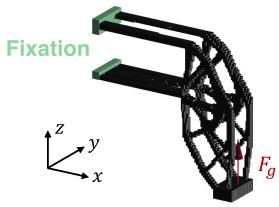

Fig. 5. Loading cases for the synthesized leg model in the standing situation. Here, the optimized density model for $\gamma = 0.08$ is used for illustration.

B. Design Stage II: Optimization of Leg Volume Fraction

In Design stage II, we first introduced the structural compliance c_2 of the synthesized leg in its standing situation, where a low c_2 value indicates a high standing stiffness. c_2 can be determined by the following equation:

$$c_2(\gamma) = \mathbf{F}_{\text{ext},2}^{\mathbf{T}}\mathbf{u_2} \quad \text{with} \quad \mathbf{r_2}(\mathbf{F}_{\text{ext},2}, \mathbf{u_2}, \mathbf{x}_{\text{opt}}(\gamma)) = \mathbf{0} \tag{8}$$

where $\mathbf{x_{opt}}(\gamma)$ denotes the optimized density model for a certain γ value, whereas the FE analysis $\mathbf{r_2} = \mathbf{0}$ is used to calculate the displacement vector $\mathbf{u_2}$ of the synthesized leg in its standing situation. The loading cases for the standing situation are shown in Fig. 5, where the left end of the leg is fixed and a vertical force $F_g = 2\,\text{N}$ is applied on the foot tip to mimic the average supporting force from the ground. The load vector $\mathbf{F}_{\text{ext},2}$ is generated from F_g.

After performing the topology optimization process from Design stage I using different γ values ($\gamma \in [0.04, 0.6]$), we summarized the optimized g_1 values (denoted by $c_1 = g_{1,\text{opt}}$) and the c_2 values calculated by (8), as shown in Fig. 6(a). Here, $\gamma_{\min}$ was chosen to be 0.04 because this is the smallest γ value that produces a reasonable and continuous bending leg structure. Since the nondesign void domain occupies about 40% volume of the entire design domain, we set the upper bound of the reachable volume fraction ($\gamma_{\max}$) as 0.6. It can be noticed from Fig. 6(a) that c_2 decreases (c_1 increases) monotonically as γ increases. In order to achieve the optimal soft-rigid hybrid performance of the synthesized leg, we created the following optimization problem for the second design stage:

$$\left.\begin{aligned} \min_{\gamma\in[\gamma_{\min},\gamma_{\max}]} \quad & : g_2(\gamma) = \varepsilon_1 + \varepsilon_2 \\ \text{s.t.} \quad & : \varepsilon_1 = \frac{c_1(\gamma) - c_{1,\min}}{c_{1,\max} - c_{1,\min}} \\ & : \varepsilon_2 = \frac{c_2(\gamma) - c_{2,\min}}{c_{2,\max} - c_{2,\min}} \end{aligned}\right\} \tag{9}$$

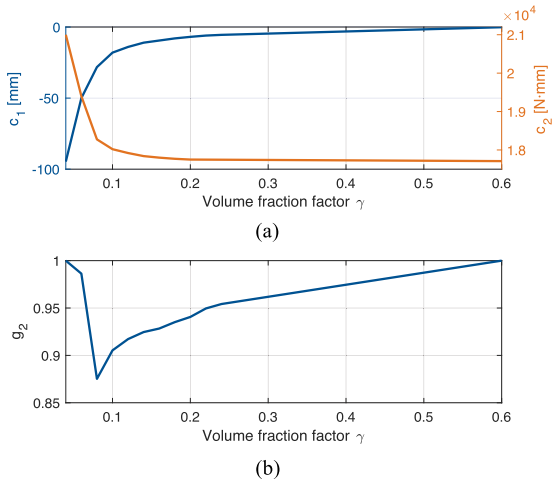

Fig. 6. (a) Diagram showing the relationship between c_1, c_2, and γ. (b) Diagram showing the relationship between g_2 and γ.

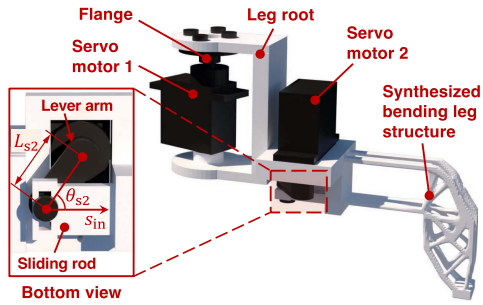

Fig. 7. Structure of a right-side robotic leg for TurBot.

where ε_1 and ε_2 are the normalized value of c_1 and c_2, respectively. By searching for the minimum value of the objective function g_2, our goal is to find a γ that simultaneously brings c_1 and c_2 as close as possible to their minimum values, i.e., the maximum bending flexibility [$c_{1,\min} = c_1(\gamma_{\min})$] and the highest standing stiffness [$c_{2,\min} = c_2(\gamma_{\max})$]. The relationship between g_2 and γ is shown in Fig. 6(b). It can be seen that g_2 achieves its minimum value (0.87) when $\gamma = 0.08$. Therefore, $\gamma = 0.08$ was selected in this work as the optimal value to synthesize the soft-rigid hybrid leg structure [see Fig. 3(b)].

Fig. 7 shows the realized monolithic structure of the robotic leg. In order to realize the proximal rotating joint, the root of the leg is connected to the flange of servo motor 1 and can be rotated around the rotation axis of the motor. The synthesized soft-rigid hybrid bending structure is also constructed on the leg root and can be actuated by servo motor 2 via a sliding rod. The entire leg can be integrated into the robotic system of TurBot by mounting servo motor 1 on the robot trunk.

III. Kinematic Modeling and Motion Planning

A. Simplified Kinematic Model of the Robotic Leg

To achieve motion planning of the created soft leg, a simple-yet-efficient kinematic model is required. After performing FE

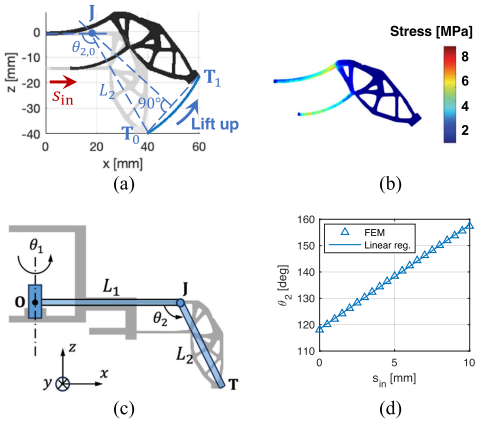

Fig. 8. (a) FE-simulated deformation of the bending leg. (b) FE-simulated stress distribution. Here, the stress level is much lower than PA2200's flexural strength (58 MPa). (c) Simplified kinematic model. (d) θ_2–s_{in} curve.

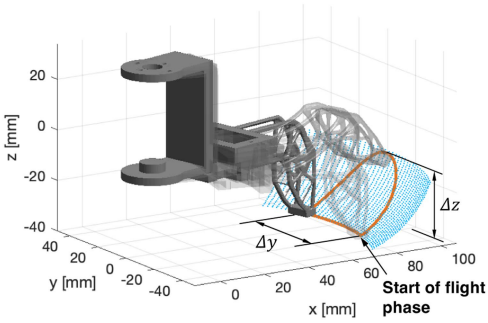

Fig. 9. Foot tip trajectory of a right-side robotic leg. Here, the blue points represent the 2-D workspace of the foot tip.

analysis [see Fig. 8(a) and (b)], we can see that, for a motor-induced displacement $s_{in} = 10$ mm ($F_{in} = 1$ N), the lift-up motion of the foot tip $\mathbf{T}$ can be approximated as a circular arc $\overset{\frown}{\mathbf{T_0T_1}}$ with its center on the x-axis, and the stresses in the leg are evenly distributed along the flexible beams. Based on this feature, we used a simplified 2-DOF rigid-link model [see Fig. 8(c)] to describe the leg kinematics. Herein, $\mathbf{O}$ and $\mathbf{J}$ represent the proximal rotating joint and the simplified bending joint, respectively. As Fig. 8(a) shows, $\mathbf{J}$ can be determined as the intersection point of the perpendicular bisector of $\overline{\mathbf{T_0T_1}}$ with the x-axis. The length of $\overline{\mathbf{JT}}$ is thus obtained as $L_2 = 44.9$ mm [see $\overline{\mathbf{JT_0}}$ in Fig. 8(a)]. Incorporating the length of the rigid leg root, the length of the rigid bar $\overline{\mathbf{OJ}}$ is determined as $L_1 = 64.4$ mm. As configuration variables for the rigid-link model, the z-axis rotation angle of the joint $\mathbf{O}$ is denoted by θ_1, whereas θ_2 depicts the y-axis rotation angle of the joint $\mathbf{J}$. Based on the FE results in Fig. 8(a), θ_2 can be determined as the angle between $\overline{\mathbf{JT}}$ and the x-axis, and we have calculated the θ_2 value for 21 $\mathbf{T}$ positions along the lift-up curve, as Fig. 8(d) shows. It can be noticed that the relationship between θ_2 and s_{in} is almost linear. Therefore, we performed a linear regression and obtained the following equation for θ_2 and s_{in}:

$$s_{in} = k_a \cdot (\theta_2 - \theta_{2,0}) \tag{10}$$

where $k_a = 0.24$ mm/° is the approximated linear factor. $\theta_{2,0} = 118.4°$ is the initial value of θ_2. In addition, according to Fig. 7, the relationship between s_{in} and the actuation angle θ_{s2} of servo motor 2 can be formulated as follows:

$$s_{in} = L_{s2} \cdot (\cos\theta_{s2,0} - \cos\theta_{s2}) \tag{11}$$

where $L_{s2} = 12$ mm is the lever arm of servo motor 2, and $\theta_{s2,0} = 54°$ is the initial value for $s_{in} = 0$ mm. Since the leg root is directly connected to the flange of servo motor 1, θ_1 is equal to the motor rotation angle θ_{s1}. Substituting (10) into (11), the relationship between the motor angles (θ_{s1} and θ_{s2}) and the configuration variables (θ_1 and θ_2) can be obtained as follows:

$$\boldsymbol{\theta}_s = \begin{bmatrix}\theta_{s1}\\ \theta_{s2}\end{bmatrix} = \begin{bmatrix}\theta_1\\ \arccos\left(\cos\theta_{s2,0} - \frac{k_a}{L_{s2}} \cdot (\theta_2 - \theta_{2,0})\right)\end{bmatrix} \tag{12}$$

where the actuation range of $\boldsymbol{\theta}_s$ is set to $\theta_{s1} \in [-30°, 30°]$ and $\theta_{s2} \in [54°, 106°]$ due to the mechanical constraints of the leg.

Based on the geometrical relationship shown in Fig. 8(c), the forward kinematics of the simplified rigid-link model can be expressed as follows:

$$\begin{bmatrix}x_T\\ y_T\\ z_T\end{bmatrix} = \begin{bmatrix}(L_1 - L_2\cos\theta_2)\cdot\cos\theta_1\\ (L_1 - L_2\cos\theta_2)\cdot\sin\theta_1\\ -L_2\sin\theta_2\end{bmatrix} \tag{13}$$

where $\begin{bmatrix}x_T & y_T & z_T\end{bmatrix}^T$ is the coordinate of the foot tip $\mathbf{T}$. According to (13), the inverse kinematics can also be derived as follows:

$$\begin{bmatrix}\theta_1\\ \theta_2\end{bmatrix} = \begin{bmatrix}\arcsin\left(\frac{y_T}{L_1+\sqrt{{L_2}^2-{z_T}^2}}\right)\\ \pi + \arcsin\left(\frac{z_T}{L_2}\right)\end{bmatrix}. \tag{14}$$

Here, only y_T and z_T are used in the calculation of inverse kinematics because the workspace of $\begin{bmatrix}x_T & y_T & z_T\end{bmatrix}^T$ is a 2-D surface, and the value of x_T can always be determined by the other two variables (y_T and z_T).

B. Foot Tip Trajectory

Mimicking the lifting and stepping motion of a turtle leg, we have designed a foot tip trajectory for the right-side robotic leg as shown in Fig. 9, which consists of a flight phase and a stance phase. Here, the y-axis and z-axis coordinates of the trajectory (orange) can be described by the following:

$$y_T(t) = \begin{cases}\Delta y \cdot \left(\frac{t}{T_f} - \frac{\sin\left(\frac{2\pi t}{T_f}\right)}{2\pi}\right) + y_0, & t \in [0, T_f]\\ \Delta y \cdot \frac{T-t}{T-T_f} + y_0, & t \in [T_f, T]\end{cases}. \tag{15}$$

$$z_T(t) = \begin{cases}\Delta z \cdot \left(\frac{1-\cos\left(\frac{2\pi t}{T_f}\right)}{2}\right) + z_0, & t \in [0, T_f]\\ z_0, & t \in [T_f, T]\end{cases}. \tag{16}$$

It can be seen from (15) and (16) that the trajectory projects a cycloid curve on the yz-plane during the flight phase, where $\Delta y =$

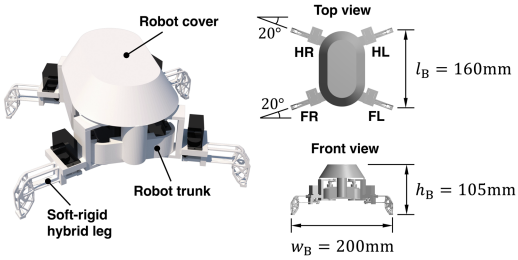

Fig. 10. Overview of the assembled robot system of TurBot. l_B, w_B, and h_B represent the overall length, width, and height of the robot body.

40 mm and $\Delta z = 25$ mm represent its maximum length in y-axis and z-axis, respectively. $y_0 = -20$ mm and $z_0 = -40$ mm denote the start position of the foot tip during a stride cycle. T is the period of a stride cycle, whereas the time T_f for the flight phase is $0.25\,T$ [24].

C. System Design of TurBot

Fig. 10 shows the created TurBot, where the four robotic legs are integrated by mounting their proximal servo motors on the robot trunk. Here, the front-left (FL) and hind-left (HL) legs are mirrored structures of the front-right (FR) and hind-right (HR) legs. Since the turtle's front and hind legs are usually in nonparallel poses to enhance its motion stability [24], we also set a 40° angle between the neutral position of TurBot's front and hind legs. In this work, the legs and body of TurBot were fabricated using selective laser sintering technology (EOS GmbH, Germany) and PA2200 material. The Arduino Micro board was chosen as micro controller to control the eight MG90S servo motors (maximum torque: 100 N · mm) of four legs. A signal receiver (REELY, Conrad, Germany) was integrated in TurBot so that it can be remotely controlled by a joystick. In addition, an 1100-mAh rechargeable lithium polymer (Li-Po) battery (URGENEX, China) was selected to power the controller board and the motors. The entire robot weighed 395 g (including the electronic components).

D. Motion Gaits

In this work, we have designed two kinds of motion gaits for TurBot, i.e., straight-line walking and turning motions.

1) Walking: By substituting (15) and (16) into (14) and (12), the control signals $\boldsymbol{\theta}_s(t) = \begin{bmatrix}\theta_{s1}(t) & \theta_{s2}(t)\end{bmatrix}^T$ for the servo motors of a leg can be calculated. Fig. 11 shows one cycle of the obtained $\boldsymbol{\theta}_s(t)$, where the first $0.25\,T$ and the latter $0.75\,T$ represent the flight and stance phases, respectively. In order to achieve a stable straight-line walking motion, we generated the control signals for different legs ($\boldsymbol{\theta}_s^{FR}$, $\boldsymbol{\theta}_s^{HL}$, $\boldsymbol{\theta}_s^{FL}$, $\boldsymbol{\theta}_s^{HR}$) as in (17) by imitating the walking pattern of a turtle [24], which moves its legs in the order of FR → HL → FL → HR

$$\begin{bmatrix}\boldsymbol{\theta}_s^{FR}\\ \boldsymbol{\theta}_s^{HL}\\ \boldsymbol{\theta}_s^{FL}\\ \boldsymbol{\theta}_s^{HR}\end{bmatrix} = \begin{bmatrix}\boldsymbol{\theta}_s(t)\\ \boldsymbol{\theta}_s(t-0.25\,T)\\ \boldsymbol{\theta}_s(t-0.5\,T)\\ \boldsymbol{\theta}_s(t-0.75\,T)\end{bmatrix}. \tag{17}$$

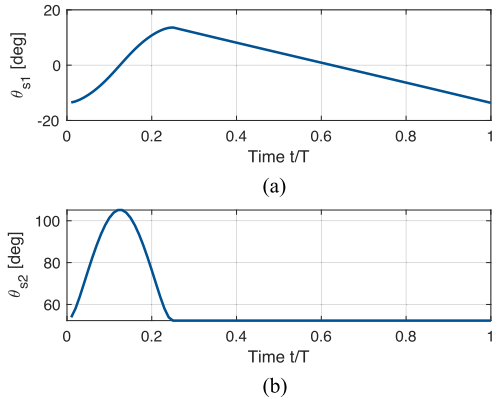

Fig. 11. Control signals for the servo motors to achieve the foot tip trajectory in Fig. 9. (a) $\theta_{s1}(t)$ for servo motor 1. (b) $\theta_{s2}(t)$ for servo motor 2.

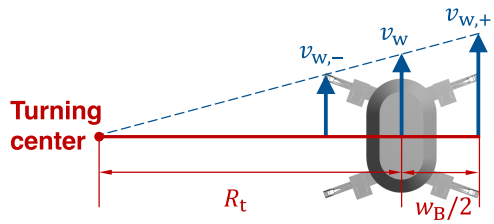

Fig. 12. Diagram illustrating the speed difference between the left-side and right-side legs of TurBot during a left-turn motion.

Herein, the phase offset between two legs is set to $0.25\,T$ to ensure that the robot is always balanced with three legs in the stance phase during walking. Since the robot can move forward $\Delta y \cdot \cos(20°)$ during a stance phase (according to Figs. 9 and 10), its walking speed v_w can be calculated as follows:

$$v_w = \frac{\Delta y \cdot \cos(20°)}{0.75\,T} = \Delta l_{st} \cdot f \tag{18}$$

where $f = 1/T$ denotes the user-defined walking frequency, and $\Delta l_{st} = 50.1$ mm indicates a stride length.

2) Turning: The turning motion of TurBot can be realized by setting a speed difference between the left-side and right-side legs. Here, we take the left-turn motion for illustration (see Fig. 12), where the walking speed of the right-side legs is increased to $v_{w,+}$ by multiplying a gain factor k_+ to their control signal $\theta_{s1}(t)$. According to (13), Δy can be expressed as $\Delta y = 2 \cdot (L_1 + \sqrt{{L_2}^2 - {z_0}^2}) \cdot \sin(\theta_{s1,max})$, where $\theta_{s1,max}$ is the maximum value of $\theta_{s1}(t)$ in Fig. 11(a). Hence, with (18), the relationship between $v_{w,+}$ and v_w can be formulated as follows:

$$\frac{v_{w,+}}{v_w} = \frac{\Delta y_+}{\Delta y} = \frac{\sin(k_+ \cdot \theta_{s1,max})}{\sin(\theta_{s1,max})} \tag{19}$$

where Δy_+ denotes the increased Δy. Similarly, the walking speed of the left-side legs can be reduced to $v_{w,-}$ by introducing another gain factor k_- as follows:

$$v_{w,-} = \frac{\sin(k_- \cdot \theta_{s1,max})}{\sin(\theta_{s1,max})} \cdot v_w. \tag{20}$$

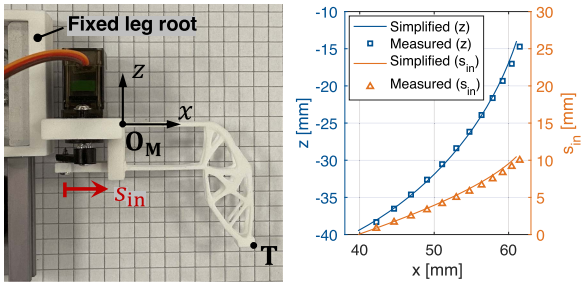

Fig. 13. (a) Experimental setup of the bending test. (b) Relationship between tip positions and s_{in} during the bending motion. Here, the measured values and the theoretical values of the simplified model were both presented.

Since we want to keep the center speed of TurBot at v_{w} (see Fig. 12), the following relationship is obtained:

$$v_{\text{w,+}} + v_{\text{w,-}} = 2 \cdot v_{\text{w}}. \tag{21}$$

Substituting (19) and (20) into (21), $k_{\text{-}}$ can be calculated as follows:

$$k_{\text{-}} = \frac{\arcsin\left(2 \cdot \sin\left(\theta_{\text{s1,max}}\right) - \sin\left(k_{\text{+}} \cdot \theta_{\text{s1,max}}\right)\right)}{\theta_{\text{s1,max}}}. \tag{22}$$

On the other hand, since the relationship between the turning radius R_{t} and w_{B} can be derived from Fig. 12 as follows:

$$\frac{R_{\text{t}}}{\frac{1}{2}w_{\text{B}}} = \frac{v_{\text{w}}}{v_{\text{w,+}} - v_{\text{w}}}. \tag{23}$$

R_{t} is determined by substituting (19) into (23) as follows:

$$R_{\text{t}}(k_{\text{+}}) = \frac{\frac{1}{2}w_{\text{B}} \cdot \sin\left(\theta_{\text{s1,max}}\right)}{\sin\left(k_{\text{+}} \cdot \theta_{\text{s1,max}}\right) - \sin\left(\theta_{\text{s1,max}}\right)}. \tag{24}$$

IV. Experiments

A. Bending Motion Test of the Synthesized Leg Structure

The first experiment was conducted to evaluate the model accuracy of the simplified bending leg structure. The experimental setup is shown in Fig. 13(a), where the leg root was fixed and the synthesized bending structure was actuated by a servo motor using different input displacement values (s_{in}). Here, $\mathbf{O}_{\text{M}}$ indicates the coordinate origin of the measurement process, whereas the deflection positions of the foot tip $\mathbf{T}$ were measured by a digital microscope (DigiMicro 2.0, Toolcraft AG, Germany). The bending test was repeated three times and the mean values were presented in Fig. 13(b). It can be noticed that the measured deflection positions were very close to the bending curve of the simplified model (solid line), and the maximum error was only 0.8 mm. Based on this result, the accuracy of the simplified kinematic model was verified.

B. Load Test of the Synthesized Leg Structure

To evaluate the load-bearing performance of the synthesized leg structure, a load test was performed as shown in Fig. 14(a). It can be seen that the leg was set in the standing pose ($s_{\text{in}} = 0$ mm)

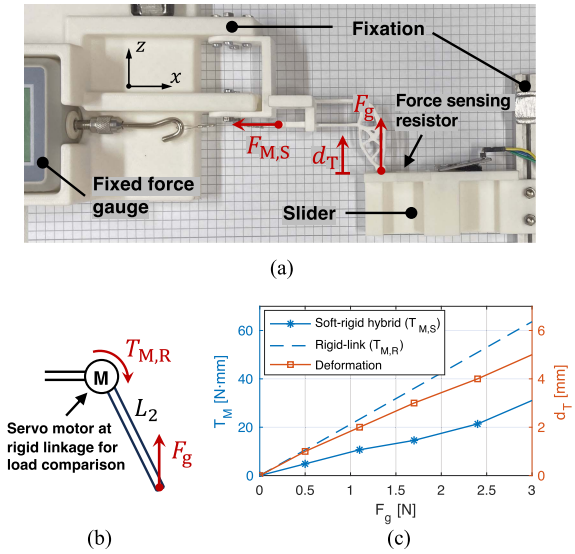

Fig. 14. (a) Experimental setup of the load test. (b) Virtual rigid-link leg mechanism for motor load comparison. (c) Relationship between $T_{\text{M,S}}$, $T_{\text{M,R}}$, d_T, and F_g. The test was repeated three times and the mean values were presented.

in the experiment since the external ground force mainly acts on the leg in this pose. To imitate the ground force, a slider was used to push the foot tip with a vertical force F_g. F_g and the foot tip movement d_T were measured by a force sensing resistor (FSRTEK, China) and a digital microscope, respectively. A fixed force gauge (SF-500, Tripod Instrument Manufacturing Company Ltd., China) was used to hold the standing pose of the leg and to measure the force $F_{\text{M,S}}$ on the sliding rod. $F_{\text{M,S}}$ was taken as the force applied to the motor, and the motor torque can be calculated as $T_{\text{M,S}} = F_{\text{M,S}} L_{\text{s2}} \sin\theta_{\text{s2,0}}$ (according to Fig. 7). In addition, based on the simplified kinematic model in Fig. 8(c), we also created a virtual rigid-link mechanism [see Fig. 14(b)] for motor load comparison, where the motor was mounted on the rotation joint to generate bending torque ($T_{\text{M,R}} = -F_g L_2 \cos\theta_{\text{2,0}}$). Fig. 14(c) shows the relationship between the measured d_T, $T_{\text{M,S}}$, and the reference torque $T_{\text{M,R}}$. It can be noticed that, although both $T_{\text{M,S}}$ and $T_{\text{M,R}}$ increased with F_g, the growth rate of $T_{\text{M,S}}$ was much slower than $T_{\text{M,R}}$, which shows the advantage of the synthesized leg structure in preventing actuation motor from being blocked by large external forces. This phenomenon can be attributed to the multiple flexible beams of the soft leg structure, as it absorbs and redistributes the load in the leg so that the load is not concentrated on the motor. On the other hand, d_T–F_g curve shows that the foot tip deflected less than 5 mm under 3 N external load, which also demonstrates the optimized standing stiffness of the soft robotic leg.

C. Tests of Different Motion Gaits of TurBot

1) Walking: In this section, walking tests were conducted to evaluate the feasibility of the proposed straight-line walking gait of TurBot. During the test, the robot was actuated to walk a distance of $D = 3$ m on a linoleum floor. Here, the linoleum floor

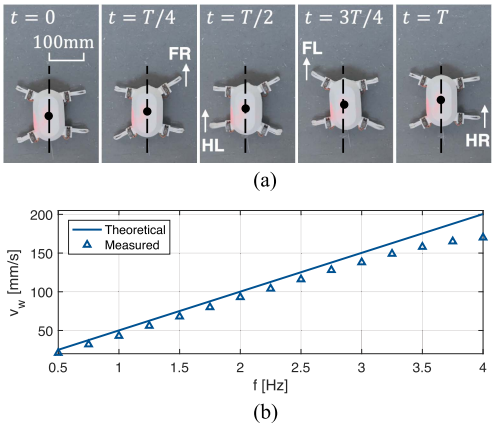

Fig. 15. (a) Walking poses of TurBot at different time points of a stride cycle. The dashed line represents the reference straight line. (b) Relationship between v_{w} and f. Here, both theoretical and measured values of v_{w} were plotted.

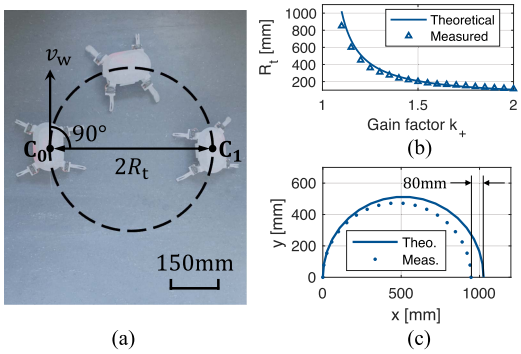

Fig. 16. (a) Measurement of the turning radius R_{t} of TurBot during a right-turn motion with $k_+ = 1.52$. (b) Relationship between R_{t} and k_+. Here, both theoretical and measured values of R_{t} were plotted. (c) Theoretical and measured turning curve for $k_+ = 1.2$ (40 mm deviation of R_{t}).

was chosen because of its high friction coefficient. Fig. 15(a) shows the walking poses of TurBot during a stride cycle. It can be seen that, by imitating the walking pattern of a turtle, the robot can stably move forward in a straight line. After measuring the walking time t_{w} (mean value of three repeated tests) for different walking frequency f, we calculated the straight-line walking speed as $v_{\mathrm{w}} = D/t_{\mathrm{w}}$ and presented the results in Fig. 15(b). It can be noticed that, for $f \leqslant 3$ Hz, the measured v_{w} was close to its theoretical value [calculated from (18)] and the maximum error was only 9.7 mm/s, which reflects the high mechanical stability of the proposed robot system and soft-rigid hybrid legs. When $f > 3$ Hz, the main reason for the large speed error was the foot tip slippage and the y-axis deformation of the leg, because the friction force from the ground became much greater when the robot moved at high speed ($v_{\mathrm{w}} > 150$ mm/s).

2) Turning: To evaluate TurBot's turning performance, we also performed turning tests, using different k_+ values to produce different turning radii R_{t}. Here, f was chosen as 1.5 Hz to maintain the walking stability, whereas the maximum k_+ was set to 2 due to the limited actuation range of θ_{s1}. Fig. 16(a) shows the principle for measuring the turning radius. First, we used a digital camera (HDR-CX240E, Sony, Japan) to measure the turning trajectory of the robot center. After determining the moving direction of the initial robot center $\mathbf{C_0}$ and its normal direction, we intersected the measured turning trajectory with the normal direction and found the position of the intersection point $\mathbf{C_1}$. Then, the distance between $\mathbf{C_1}$ and $\mathbf{C_0}$ was measured as the turning diameter ($2R_{\mathrm{t}}$). Fig. 16(b) shows the relationship between the measured R_{t} (mean value of three repeated left-turn and right-turn tests) and k_+. It can be seen that, as k_+ increased, the measured R_{t} decreased at a rate similar to its theoretical curve [calculated from (24)], which verified the feasibility of the proposed turning walking gait. Nevertheless, it can also be noticed that, when $k_+ < 1.3$, the difference between the theoretical and measured R_{t} was greater than 30 mm [see the $k_+ = 1.2$ example in Fig. 16(c)]. The main reason for this phenomenon is that the R_{t} value is very sensitive to the change in k_+ when k_+ is small (see the theoretical curve), which makes a very small error in k_+ (due to the motor control accuracy) lead to a large deviation in R_{t}.

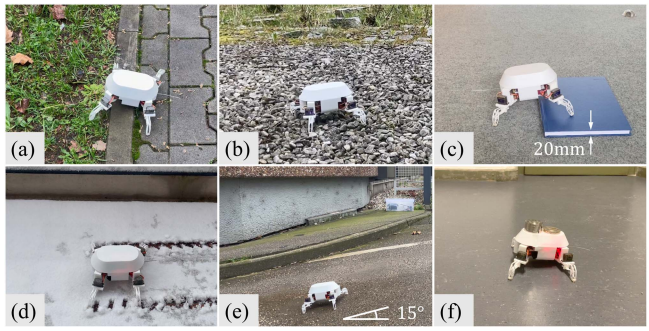

Fig. 17. Locomotion of TurBot in different environments. (a) Walking on a muddy lawn (with 20 mm stair). (b) Walking over an uneven road with stones (about 20 mm in size). (c) Climbing over a book. (d) Walking on a snowy road. (e) Climbing a slope. (f) Walking with an extra weight of 500 g.

D. Locomotion Tests in Different Environments

To evaluate TurBot's ability to adapt to different environmental conditions, a series of locomotion tests were conducted, as shown in Fig. 17. The related walking videos can also be found in the Supplementary Material. Here, f was set to 1.5 Hz for all locomotion cases. In scenario 1 and 2 [see Fig. 17(a) and (b)], the robot was able to walk over a muddy lawn and an uneven road with stones, respectively. This demonstrated the high flexibility of the synthesized soft-rigid hybrid leg and its adaptability to complex terrains. In scenario 3 [see Fig. 17(c)], the robot can climb over a book with a thickness of 20 mm, which successfully fulfilled the 20 mm obstacle-climbing requirement in Section II. In scenario 4 [see Fig. 17(d)], the robot can achieve stable straight-line walking on a snowy road with a temperature of -10 °C, which proved its mechanical reliability under extreme cold conditions. In scenario 5 [see Fig. 17(e)], the robot was able to climb up a concrete slope with an inclination angle of 15°, which demonstrated TurBot's ability to walk against resistance.

In the last scenario [see Fig. 17(f)], the robot can walk in a straight line while carrying an extra weight of 500 g (each stance leg bears about 3 N ground force in total), which validated the high load-bearing capacity of TurBot.

V. Conclusion

In this article, we presented a turtle-inspired quadruped robot (TurBot) with 3-D-printed soft legs. Using a multistage topology optimization method, the realized soft leg structure achieved balanced bending flexibility and standing stiffness. Results of locomotion tests demonstrated that the robot has stable walking performance and can successfully adapt to complex environments. Different from the underactuated legs with assembled springs and dampers [9], [10], the soft leg realized in this work had a monolithic structure that utilized the compliance of its own material to cushion external impacts, and can thus be 3-D-printed in one piece. By introducing the proximal rotating joints, the realized quadruped robot achieved greater locomotion flexibility than the 3-D-printed turtle-like soft robot in [25]. Compared with other soft quadruped robots [12], [13], TurBot showed a greater load-bearing capacity as each of its stance legs can bear about 3 N ground force while walking, which also validated the soft-rigid hybrid feature of the leg. In addition, the proposed leg outperformed the rigid-link legs with motors mounted on the rotation joints, because the multiple flexible beams in the soft leg structure redistributed the load in the leg and helped to protect the servo motor from concentrated loads (see Section IV-B). Furthermore, the design of the direct motor-driven legs also improved the actuation efficiency of the robot.

Nonetheless, this work can still be improved in several aspects. For example, a larger design domain could be employed in the optimization process to improve the obstacle-climbing performance of the synthesized leg. On the other hand, more motion gaits could also be designed in future work to further explore the multimodal locomotion potential of the robot.

Acknowledgment

The authors would like to thank Chujun Zong for her help in creating the figures and videos in this article.

References

[1] A. Fukuhara, M. Gunji, and Y. Masuda, "Comparative anatomy of quadruped robots and animals: A review," *Adv. Robot.*, vol. 36, no. 13, pp. 612–630, 2022.
[2] J. Hooks et al., "ALPHRED: A multi-modal operations quadruped robot for package delivery applications," *IEEE Robot. Autom. Lett.*, vol. 5, no. 4, pp. 5409–5416, Oct. 2020.
[3] J. Lee, J. Hwangbo, L. Wellhausen, V. Koltun, and M. Hutter, "Learning quadrupedal locomotion over challenging terrain," *Sci. Robot.*, vol. 5, no. 47, 2020, Art. no. eabc5986.
[4] Y. Li, F. Fish, Y. Chen, T. Ren, and J. Zhou, "Bio-inspired robotic dog paddling: Kinematic and hydro-dynamic analysis," *Bioinspiration Biomimetics*, vol. 14, no. 6, 2019, Art. no. 066008.
[5] Q. Shi et al., "Development of a small-sized quadruped robotic rat capable of multimodal motions," *IEEE Trans. Robot.*, vol. 38, no. 5, pp. 3027–3043, Oct. 2022.
[6] K. Melo, T. Horvat, and A. J. Ijspeert, "Animal robots in the African wilderness: Lessons learned and outlook for field robotics," *Sci. Robot.*, vol. 8, no. 85, 2023, Art. no. eadd8662.
[7] R. Baines et al., "Multi-environment robotic transitions through adaptive morphogenesis," *Nature*, vol. 610, no. 7931, pp. 283–289, 2022.
[8] Z. Tang, K. Wang, E. S.-Papastavridis, and J. S. Dai, "Origaker: A novel multi-mimicry quadruped robot based on a metamorphic mechanism," *J. Mech. Robot.*, vol. 14, no. 6, 2022, Art. no. 060907.
[9] A. Spröwitz, A. Tuleu, M. Vespignani, M. Ajallooeian, E. Badri, and A. J. Ijspeert, "Towards dynamic trot gait locomotion: Design, control, and experiments with cheetah-cub, a compliant quadruped robot," *Int. J. Robot. Res.*, vol. 32, no. 8, pp. 932–950, 2013.
[10] M. Hutter, C. D. Remy, M. A. Hoepflinger, and R. Siegwart, "Efficient and versatile locomotion with highly compliant legs," *IEEE/ASME Trans. Mechatronics*, vol. 18, no. 2, pp. 449–458, Apr. 2013.
[11] M. T. Tolley et al., "A resilient, untethered soft robot," *Soft Robot.*, vol. 1, no. 3, pp. 213–223, 2014.
[12] S. T. Muralidharan, R. Zhu, Q. Ji, L. Feng, X. V. Wang, and L. Wang, "A soft quadruped robot enabled by continuum actuators," in *Proc. IEEE 17th Int. Conf. Automat. Sci. Eng.*, 2021, pp. 834–840.
[13] D. Drotman, S. Jadhav, M. Karimi, P. d. Zonia, and M. T. Tolley, "3D printed soft actuators for a legged robot capable of navigating unstructured terrain," in *Proc. IEEE Int. Conf. Robot. Automat.*, 2017, pp. 5532–5538.
[14] Y. Sun, Y. Liu, L. Xu, Y. Zou, A. Faragasso, and T. C. Lueth, "Automatic design of compliant surgical forceps with adaptive grasping functions," *IEEE Robot. Autom. Lett.*, vol. 5, no. 2, pp. 1095–1102, Apr. 2020.
[15] C.-H. Liu, F.-M. Chung, Y. Chen, C.-H. Chiu, and T.-L. Chen, "Optimal design of a motor-driven three-finger soft robotic gripper," *IEEE/ASME Trans. Mechatronics*, vol. 25, no. 4, pp. 1830–1840, Aug. 2020.
[16] Y. Sun, Y. Liu, F. Pancheri, and T. C. Lueth, "LARG: A lightweight robotic gripper with 3-D topology optimized adaptive fingers," *IEEE/ASME Trans. Mechatronics*, vol. 27, no. 4, pp. 2026–2034, Aug. 2022.
[17] H. Zhang, A. S. Kumar, F. Chen, J. Y. H. Fuh, and M. Y. Wang, "Topology optimized multimaterial soft fingers for applications on grippers, rehabilitation, and artificial hands," *IEEE/ASME Trans. Mechatronics*, vol. 24, no. 1, pp. 120–131, Feb. 2019.
[18] Y. Sun and T. C. Lueth, "Enhancing torsional stiffness of continuum robots using 3-D topology optimized flexure joints," *IEEE/ASME Trans. Mechatronics*, vol. 28, no. 4, pp. 1844–1852, Aug. 2023.
[19] S. Chen, G. Zhou, D. Li, Z. Song, and F. Chen, "Soft robotic joints with anisotropic stiffness by multiobjective topology optimization," *IEEE/ASME Trans. Mechatronics*, vol. 29, no. 2, pp. 1064–1075, Apr. 2024.
[20] Y. Sun, C. Zong, F. Pancheri, T. Chen, and T. C. Lueth, "Design of topology optimized compliant legs for bio-inspired quadruped robots," *Sci. Rep.*, vol. 13, 2023, Art. no. 4875.
[21] Y. Sun, D. Zhang, Y. Liu, and T. C. Lueth, "FEM-based mechanics modeling of bio-inspired compliant mechanisms for medical applications," *IEEE Trans. Med. Robot. Bionics*, vol. 2, no. 3, pp. 364–373, Aug. 2020.
[22] K. Liu and A. Tovar, "An efficient 3D topology optimization code written in matlab," *Struct. Multidisciplinary Optim.*, vol. 50, no. 6, pp. 1175–1196, 2014.
[23] Y. Sun and T. C. Lueth, "SGCL: A B-Rep-based geometry modeling language in MATLAB for designing 3D-printable medical robots," in *Proc. IEEE 17th Int. Conf. Automat. Sci. Eng.*, 2021, pp. 1388–1393.
[24] J. Wyneken, K. J. Lohmann, and J. A. Musick, *The Biology of Sea Turtles*, vol. 3. Boca Raton, FL, USA: CRC Press, 2013.
[25] L. Sun, J. Wan, and T. Du, "Fully 3D-printed tortoise-like soft mobile robot with muti-scenario adaptability," *Bioinspiration Biomimetics*, vol. 18, no. 6, 2023, Art. no. 066011.

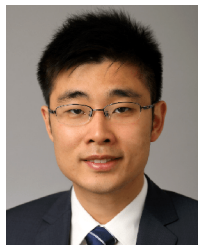

Yilun Sun (Member, IEEE) received the B.Sc. degree in mechanical engineering and automation from Shanghai Jiao Tong University, Shanghai, China, in 2013, and the M.Sc. and Dr.-Ing. degree in mechanical engineering from the Technical University of Munich (TUM), Munich, Germany, in 2017 and 2021, respectively.

He is currently a Senior Research Fellow with the Institute of Micro Technology and Medical Device Technology (MiMed) in TUM. His research interests include bio-robotics, soft robotic manipulators, medical robotics, structural-optimization-based automatic design, and 3-D-printing technologies.

Dr. Sun was the recipient of the grade *summa cum laude* for his doctor thesis. He is also a Member of the first early career editorial board in *Biomimetic Intelligence and Robotics*.

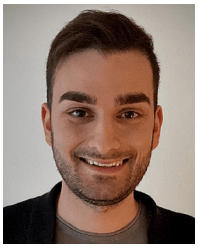

Felix Pancheri received the M.Sc. degree in mechatronics and information technology from the Technical University of Munich, Munich, Germany, in 2020, where he is currently working toward the Ph.D. degree with the Institute of Micro Technology and Medical Device Technology.

His research interests include robotics, additive manufacturing, and investment casting for optimized structures.

Christoph Rehekampff received the M.Sc. degree in mechanical engineering in 2017 from the Technical University of Munich, Munich, Germany, where he is currently working toward the Ph.D. degree in mechanical engineering with the Institute of Micro Technology and Medical Device Technology.

His research interests include additive manufacturing, mechatronic systems, and robotics.

Tim C. Lueth (Senior Member, IEEE) received the Dipl.-Ing. degree in electrical engineering from the Darmstadt University of Technology, Darmstadt, Germany, in 1989, and the Ph.D. degree in robotics and Habilitation in computer science from the University of Karlsruhe, Karlsruhe, Germany, in 1993 and 1997, respectively.

From 1994 to 1995, he was a Visiting Researcher with the MITI-AIST Electrotechnical Laboratory, Tsukuba, Japan. In 1997, he was an Associate Professor with the Humboldt University, Berlin, Germany, and in 2001, the Director of the Department of Mechatronic Medical Devices, Humboldt-University and Fraunhofer Society. In 2005, he became a Full Professor and the Director with the Department of Micro Technology and Medical Device Technology, Department of Mechanical Engineering, Technical University of Munich, Munich, Germany. His current research interests include mechatronic medical devices, surgical navigation systems for dental-, ENT-, CMF-, neuro-, and soft tissue surgery, navigated control applications, RFID, and rapid prototyping technologies.

Prof. Lueth was the recipient of several national and international awards for his research on medical devices. He became an Elected Member of “acatech” from the German National Academy for Science and Technology in 2010. He is also an Active Member of the IEEE R&A Society and the IEEE Engineering in Medicine and Biology Society.